Influence of different coil geometries on the spatial distribution of the plasma density in planar inductively coupled plasmas

A. Schwabedissen, E. C. Benck, and J. R. Roberts
National Institute of Standards and Technology, Gaithersburg, Maryland 20899
(Received 1 May 1997; revised manuscript received 24 July 1997)

The radial distributions of the electron density and the relative atomic argon excited state density have been investigated by means of Langmuir probes and optical emission spectroscopy, respectively, in planar inductively coupled plasmas. The plasma source is a modified Gaseous Electronics Conference RF Reference Cell [P. J. Hargis *et al.*, Rev. Sci. Instrum. **65**, 140 (1994)]. Two different planar coil geometries, a five-turn spiral coil and a one-turn circular coil, were investigated for a variety of plasma parameters. Additionally, we investigated the effect of different powering configurations of the spiral coil and an electrostatic shield between the coil and the plasma. We found that the coil geometry and power configuration of the coil influences the radial distribution of the electron density in the region close to the coil only, while in the region close to the lower electrode the radial distribution is dominated by diffusion. [S1063-651X(97)02811-0]

PACS number(s): 52.80.Pi, 52.70.Kz, 52.70.Ds

I. INTRODUCTION

Much attention has been paid recently to radio-frequency (rf) inductively coupled plasma (ICP) systems as innovative plasma sources for plasma processing applications in the semiconductor industry. There is a need for high density (plasma density$>10^{11}\,\mathrm{cm}^{-3}$), low pressure (0.1–5 Pa) plasma sources with high etch anisotropy and high uniformity over diameters $\geqslant 300$ mm. With conventional, capacitively coupled reactors these requirements necessitate high power to achieve sufficient throughput. However, since in diode-type reactors the ion energy and flux are coupled together, this leads to very high energies, which can cause substrate or wafer damage. A promising and relatively simple method of ICP excitation consists of using a planar coil, coupling a rf field through a quartz window into the plasma chamber [1–4]. The ion flux is controlled by the coil power, while the ion energy can in principle be independently controlled by biasing the lower electrode.

Since experience has demonstrated that experimental data from low-temperature glow discharges have often been difficult to compare when obtained by different research groups, a reference reactor for parallel plate capacitively coupled rf discharges, the Gaseous Electronics Conference (GEC) RF Reference Cell, was developed in the late 1980s. This cell has led to a much better understanding of the physical and chemical processes in parallel plate reactors [5]. Today, more than 29 of these reactors exist worldwide. Since the trend in plasma etching technology is directed towards inductively coupled plasmas, several of these cells have been modified to inductively coupled cells by replacing the standard upper electrode assembly with a spiral planar coil and a quartz vacuum interface [6–9]. This design, as in the case of the original GEC reactor, provides satisfactory technical performance and excellent diagnostic access. One drawback, however, is the rather poor radial uniformity of the plasma density in the region close to the lower electrode or wafer. At a distance of about 10 mm above the lower electrode, the electron density, measured by Langmuir probes, peaks near the chamber axis and then drops radially towards the walls [6,8]. A radial uniformity $\leqslant \pm 5\%$ is obtained for a diameter $\leqslant 50$ mm. Since the trend in semiconductor production is towards large wafer diameters of 300 mm and plasma uniformity across the substrate of better than a few percent is mandatory, this type of performance is not satisfactory.

It was first noted by Keller [10] and later calculated by Ventzek *et al.* [11] that planar ICPs with uniformly spaced spiral coils induce the largest electric field in the plasma at a radius that is roughly half the radius of the coil. If the gas pressure is low enough, so that collisionless heating dominates [12,13], the electrons are heated near the maximum field. However, the ionization occurs over a larger area and the location of maximum plasma density can move to the center of the plasma due to the heat conductivity of the electrons (nonlocal field approach), thus creating a nonuniform distribution. To correct this nonuniformity, different techniques have been reported in the literature, among them are the following.

(1) The plasma can be radially confined by multipole magnetic cusps [14–16]. This method cannot be applied to our cell because of the number and size of the radial flanges for diagnostics.

(2) The rf fields can be altered by varying the thickness of the dielectric window where the plasma density is maximum [17,18].

(3) By using a one-turn coil instead of a multiturn spiral coil Fukasawa and co-workers [19] reported a more uniform radial distribution for their ICP cell.

(4) The rf current density in the coil can be altered by adding a capacitor between the coil and ground [20].

The aim of this work is to investigate the effect of different planar coil geometries and electrical configurations on the spatial distribution of the electron density and plasma emission in an inductively coupled GEC cell (GEC-ICP cell). Our standard configuration consists of an electrostatically shielded, planar five-turn spiral coil with the center lead powered at 13.56 MHz and the outer lead grounded. Besides this five-turn spiral coil we also used a one turn-coil as de-

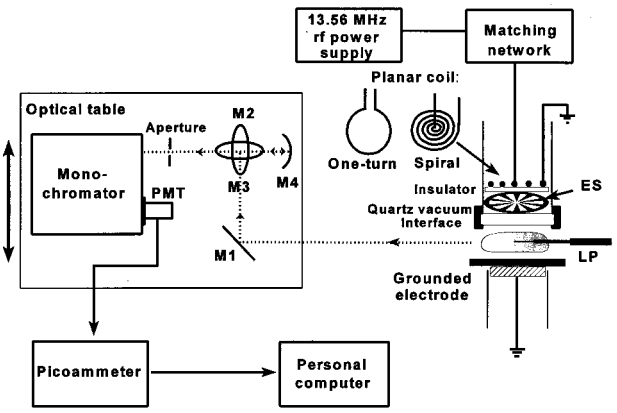

FIG. 1. Schematic diagram of the experimental setup. (LP: Langmuir probe; PMT: photomultiplier; ES: electrostatic (Faraday) shield; $M1-M4$: mirrors).

scribed by Fukasawa *et al.* [19]. Furthermore, we also investigated the effects of the electrical circuit configuration for the spiral coil by powering the outer lead and grounding the center lead, putting a capacitor between outer lead and ground and performing measurements with and without an electrostatic shield between the induction coil and plasma. All measurements were performed in pure argon by using cylindrical Langmuir probes (LP) for absolute electron density measurements and spatially resolved optical emission spectroscopy (OES) for relative electron density measurements. The radial electron density and OES profiles are also a measure of the radial profile of the ion flux to the lower electrode or substrate, since the ion flux on the substrate is determined by the radial plasma profile in the bulk plasma [21].

II. EXPERIMENTAL CONFIGURATION

A schematic of the experimental set up is shown in Fig. 1. The cylindrical vacuum chamber is constructed of stainless steel with eight radial flanges centered at the electrode midplane. Two of them are 203 mm diameter flanges fitted with 136 mm diameter quartz windows for OES observation. Since a detailed sketch of the electrode region of the GEC-ICP cell has been presented previously [6], we will repeat only the most important dimensions: (1) inner diameter of the cell chamber of 251 mm; (2) diameter of the stainless steel lower electrode plate of 165 mm; (3) distance l between the quartz vacuum interface (thickness 9.5 mm) and the lower electrode of 40.5 mm. Because the quartz vacuum interface is held in place by a stainless steel flange, the observable vertical distance of the plasma from the lower electrode is 34.1 mm.

Two different types of coils were examined: one a uniformly spaced, five-turn spiral coil with outer diameter 100 mm, inductance 1.1 ± 0.1 μH and the other a one-turn circular coil with an outer diameter of 100 mm and an inductance 0.55 ± 0.05 μH. Both coils were made of 3 mm (1/8 in) copper tubing and water cooled during discharge operation. Between the coil and the radially spoked Faraday shield [22] a 3 mm thick quartz plate was mounted for electrical insulation. Therefore, the total distance between coil and lower electrode is approximately 53 mm. The spiral coil is held rigidly in place by a slotted five arm holder, which was mounted on top of the cell. The coil voltage V_{coil} was measured by a capacitive voltage probe and the current I_{coil} by an inductively coupled current probe. The data are presented as a function of the plasma power, which is the difference between the total input power and resistive losses $I_{\mathrm{coil}}^2 R_{\mathrm{eff}}$ [8]. R_{eff} is the effective resistance of the coil and surrounding hardware (spiral coil: $R_{\mathrm{eff}}=0.7\,\Omega$; one-turn coil: $R_{\mathrm{eff}}=0.34\,\Omega$), measured with no plasma present.

The absolute electron density was measured by a commercial, passively compensated, cylindrical LP with a probe tip radius of 190 μm and a tip length of 6 mm. The probe assembly was attached to a manually operated x-y-z manipulator, which was mounted to one of the 70 mm side flanges of the cell chamber. The Druyvesteyn method, that is, the relation between the electron energy distribution function (EEDF) and the second derivative of the current-voltage characteristic $I''(U)$, was used to calculate the electron density, N_e [23,24], by integrating over the second derivative according to

$$n_e=\left(\frac{8m_e}{e^3}\right)^{1/2}\frac{1}{A_{\mathrm{pr}}}\int_{-\infty}^{0}\sqrt{-U}I''(U)dU, \tag{1}$$

where e and m_e are the charge and mass of an electron, A_{pr} the probe surface area, $U=U_{\mathrm{pr}}-U_{\mathrm{pl}}$ and U_{pr} is the probe voltage and U_{pl} the plasma potential. The plasma potential was determined from the zero crossing of the second derivative of the current-voltage characteristic. By averaging up to ten current-voltage probe characteristics we found a relative standard uncertainty σ (given by statistical errors) of the electron density for each data point within a radial scan of less than 4%. Taking into account the uncertainty of the probe surface area (with a systematic error of 6%) the total relative standard uncertainty of the electron density amounts to 10%.

The OES setup is also shown schematically in Fig. 1. The discharge is imaged onto the slit of a 1 m grating monochromator by a system of mirrors $M1$ to $M4$. These mirrors act as a periscope, rotating the plasma image by 90°. The entrance slit of the monochromator is typically 50–100 μm wide and 2 mm high. The monochromator is equipped with a cooled photomultiplier. A picoammeter measures the time averaged photomultiplier current. The spatial resolution is 0.4 mm vertically and 4 mm horizontally. The data acquisition system is operated and controlled by a computer. Scanning of the plasma emission in the axial direction is accomplished by translating one of the mirrors of the periscope. Lateral scanning of the plasma emission is accomplished by translating the entire OES detection system, which is mounted on a movable table. In order to convert these lateral, line-of sight-integrated observations into a radial distribution, the data had to be Abel inverted. Since the emission did not decrease to zero at $y=\pm68$ mm (radius of the observation window), an exponential function $f(y)=B\exp[-a(y-y_0)]$ was fit to the edges of the raw data. An overview of different methods for numerical Abel inversion is given by Pretzler *et al.* [25]. We used a method that interpolates the radial distribution with even order polynomials.

Three Ar I lines at 750.39 nm ($2p_1 \rightarrow 1s_2$), 451.07 nm ($3p_5 \rightarrow 1s_2$), and 383.47 nm ($4p_5 \rightarrow 1s_2$) were observed. The optical mean free path for all three transitions was estimated by using the measured $1s_2$ densities and neutral temperatures from Hebner's work [26] and the transition probabilities of Wiese *et al.* [27]. The calculated optical mean free paths are 0.23, 37, and 94 m for the 750.39, 451.07, and 383.47 nm transition, respectively. Since none of the optical mean free paths is significantly less than the physical dimensions of the plasma, optical trapping has not been taken into account in the data evaluation of the OES measurements. We investigated predominantly the Ar I transition line at 750.39 nm ($2p_1 \rightarrow 1s_2$). No significant variation between normalized Abel inverted OES signals was obtained when observing the two other Ar I lines at 451.07 and 383.47 nm. We estimated the electron collision excitation rates to the $2p_1$ level (with an excitation energy of 13.47 eV) from the ground state of argon, from the resonance level $1s_2$ and from the metastable level $1s_5$. By using typical measured electron densities (1×10^{11} cm^{-3}) [8], effective temperatures (4 eV) [6,8] and argon exited state densities [26] for this ICP reactor at a pressure of 1.33 Pa and using the calculated electron collision excitation cross sections of Clark *et al.* [28] we obtained the following excitation rates to the $2p_1$ level: 3×10^{14} cm^{-3} s^{-1} for the excitation from ground state, 4.4×10^{12} cm^{-3} s^{-1} for the excitation from the resonance state $1s_2$ and 5×10^{11} cm^{-3} s^{-1} for the excitation from the metastable state $1s_5$. These rates show that the excitation from the ground state is the dominant excitation process for the $2p_1$ population. Therefore, assuming that the neutral gas density is spatially uniform, the OES signal is proportional to the density of electrons with energies greater than 13.47 eV.

III. EXPERIMENTAL RESULTS

All measurements were performed in pure argon in the pressure range from 0.33 to 4 Pa (2.5 to 30 mTorr). The standard gas flow rate was 3.7 μmol/s [5 SCCM (SCCM denotes cubic centimeter per minute at STP)]. Radial scans of the electron density, measured by the LP, were performed at a distance of 12 mm above the lower electrode (41 mm below the coil), while radially resolved OES measurements were made in intervals of 4–5 mm between the lower electrode and the quartz vacuum interface flange.

A. Comparison between one-turn coil and five-turn spiral coil

The rf voltages, currents (peak-to-peak values), plasma powers, and plasma coupling efficiencies in the inductive discharge mode for both coil geometries are presented in Fig. 2. The total input power was 150 W for the spiral coil and 300 W for the one-turn coil, which resulted in similar plasma power, since the resistive losses $I_{\text{coil}}^2 R_{\text{eff}}$ are higher for the one-turn coil. The plasma coupling efficiency η ($=P_{\text{dis}}/P_{\text{in}}$) is a factor of two smaller for the one-turn coil compared to the spiral coil.

Radially resolved LP measurements of the electron density for each coil geometry, normalized to their maximum values, are shown in Fig. 3. The half-width at half maximum of the radial electron density profile increases from 40 mm at 4 Pa to 50 mm at 0.5 Pa, but in contrast to the results of

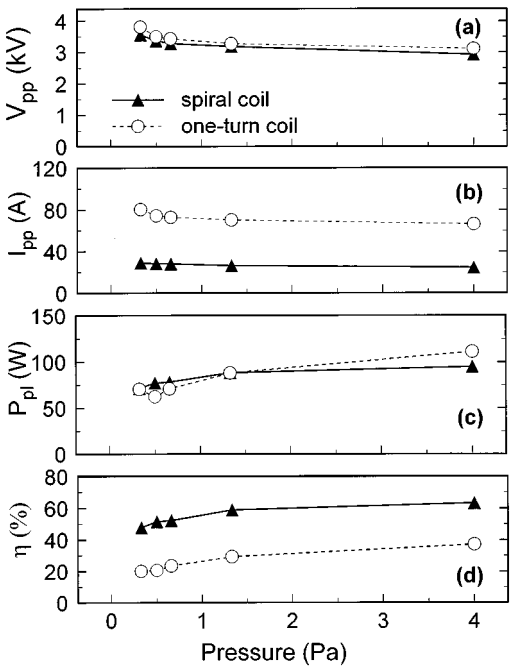

FIG. 2. Peak-to-peak values of (a) coil voltage, (b) current, (c) power deposited into the plasma P_{dis}, and (d) coupling efficiency η in percent for the two coil geometries as a function of the gas pressure.

Fukasawa and co-workers [19], we do not observe a more uniform radial distribution when using a one-turn coil instead of a spiral coil (see Fig. 4). Figure 4(a) shows a comparison of our data with the results of Miller *et al.* [6], who also performed his experiments at a GEC-ICP cell. The agreement with Miller's data is very good. The reason for the

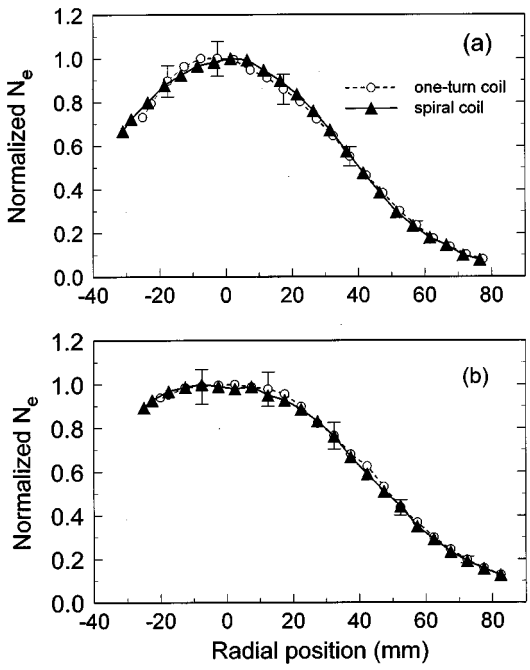

FIG. 3. Normalized electron density at a distance of 12 mm above the lower electrode for both coil geometries at (a) $p=4$ Pa and (b) $p=0.5$ Pa.

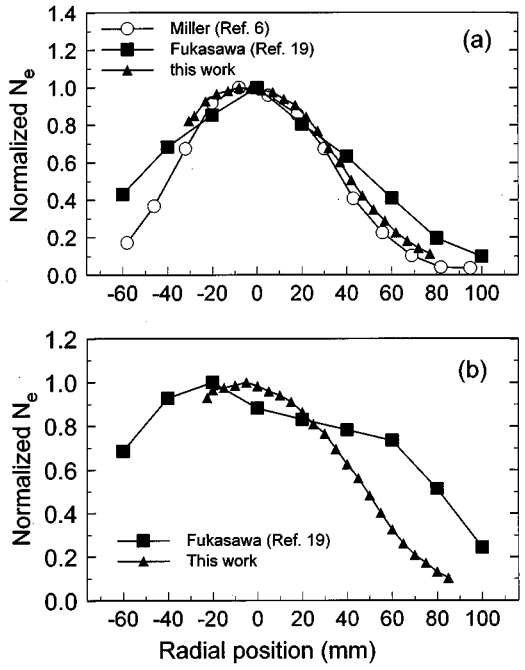

FIG. 4. Comparison of normalized electron densities in different ICP cells at $p = 1.33$ Pa for (a) a five-turn spiral coil and (b) a one-turn coil.

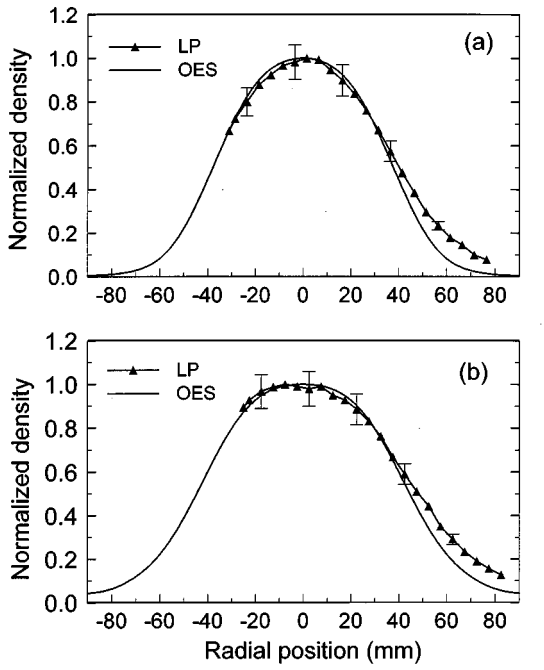

FIG. 5. Comparison of normalized, Abel inverted OES signals at 750.4 nm with normalized electron densities, obtained by Langmuir probe at (a) $p = 4$ Pa and (b) $p = 0.5$ Pa for the spiral coil.

discrepancy to the results of Fukasawa *et al.* when using a one-turn coil instead of a spiral coil [Fig. 4(b)] is probably due to the design of the GEC-ICP cell. The induction coil is surrounded by a stainless steel tube of 113 mm inner diameter with a copper liner (see Fig. 1 and Ref. [6]). The outer turn of the coil is placed less than 7 mm from the cylinder wall, which becomes hot during discharge operation, a clear indication of induced currents in the wall. Because the one-turn coil requires more current to produce the same plasma power, the induced currents in the cylinder wall are higher for the one-turn coil than for the five-turn spiral coil. It is likely that the image current in the wall is equal to the coil current, thus having a considerable effect on the plasma in the region close to the quartz vacuum interface. In contrast to our GEC-ICP cell, the cell design of Fukasawa *et al.* [19] does not have such a close distance between coil (diameter 160 mm) and surrounding wall. Their coil is placed upon a quartz plate 230 mm in diameter, resulting in a distance of about 35 mm between coil and surrounding metal wall and therefore in much smaller induced wall currents. It should be mentioned that Fukasawa and co-workers observed a more uniform radial distribution in discharge regions up to 45 mm below the induction coil [19], while for the GEC-ICP cell the influence of the coil is limited to a region of about 20–25 mm below the coil.

Figure 5 shows a comparison of the normalized radial electron density, obtained with the LP, and Abel inverted lateral OES measurements. The agreement between the two signals is very good. The largest deviation can be found in the wings of the profile. The upper state $(2p_1)$ density of the investigated transition depends not only on the local electron density but also on the electron temperature or, to be more specific, the EEDF. It has been observed in another series of LP measurements [6,8] that the effective electron temperature is constant over a region corresponding to the coil diameter, but then drops towards the wall. Therefore, the two signals can be expected to deviate in the outer discharge regions due to the temperature distribution. It should also be mentioned that the fit of the line-of-sight integrated OES data beyond the range of available data ($y > 68$ mm) can lead to a distortion in the Abel inverted data if the real emission is not well fit by an exponential function.

Since we are not necessarily interested in absolute electron densities but in relative radial density profiles, the OES method offers several advantages over LP measurements. Firstly, it is a nonintrusive, passive method, which does not disturb the plasma. Secondly, it offers the possibility to measure radial distributions in areas that cannot be reached by the probe due to geometrical obstacles like the finite diameter of the probe shaft (6 mm) and the limited vertical translation length (25 mm) of the x-y-z manipulator. This especially concerns the upper discharge region close to the quartz vacuum interface. Therefore, all following graphs show the results of the OES measurements only. LP measurements have been performed for comparison and good agreement was found.

Figures 6 and 7 show Abel inverted OES signals at different distances from the lower electrode for the spiral coil and the one-turn coil, respectively. In each of these figures the data are plotted for two different pressures. The largest OES signal is observed approximately 25–28 mm above the lower electrode (or 12–15 mm below the quartz vacuum interface). The radial distribution of the OES signal when using the spiral coil (Fig. 6) shows the widest plateau in the upper discharge region (close to the coil). Near the lower electrode, however, the distribution peaks at the discharge

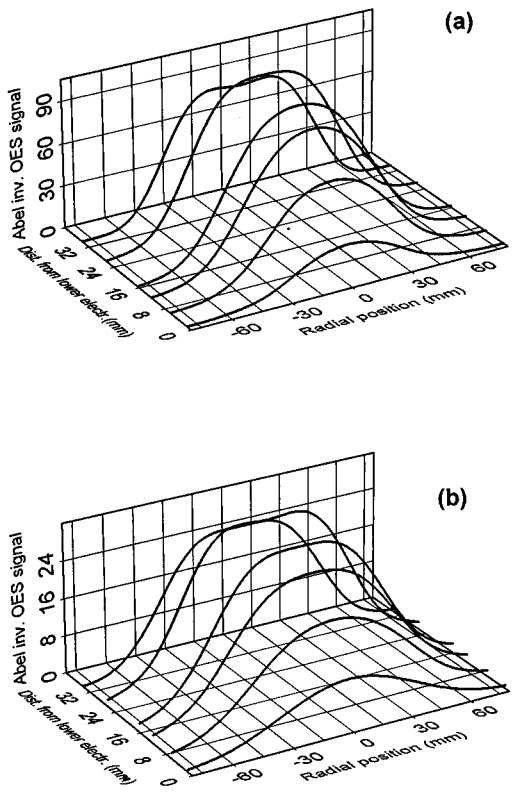

FIG. 6. Abel inverted OES signals for different distances from the lower electrode at (a) $p=4$ Pa and (b) $p=0.5$ Pa for the spiral coil.

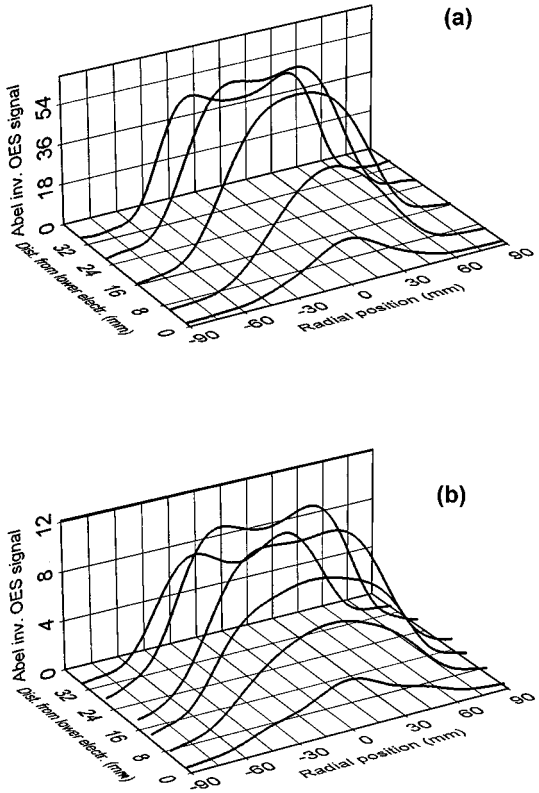

FIG. 7. Abel inverted OES signals for different distances from the lower electrode at (a) $p=4$ Pa and (b) $p=0.5$ Pa for the one-turn coil.

axis and then drops towards the wall. The width of the plateau in the upper discharge regions increases with decreasing pressure. In the case of the one-turn coil (Fig. 7), the radial OES distributions in the upper discharge region show a pronounced maximum at approximately one-half the coil radius. Near the lower electrode, however, the maximum is at the discharge center, as in the case of the spiral coil.

The off-axis density peak in the upper discharge region, close to the quartz vacuum interface, can be understood in terms of the radial distribution of the induced electric field. As discussed by Hopwood *et al.* [29], the inductive electric field peaks at approximately one-half the radius of the induction coil r_{coil} and goes to zero at the center of the discharge. The absorbed power is proportional to the square of the electric field and therefore also peaks at $\sim r_{\mathrm{coil}}/2$. On the other hand, the axial power deposition in a planar ICP can be described as an exponential decay of a cylindrical TE wave into a plasma, because the electron plasma frequency ω_{pe} is greater than 13.56 MHz, which implies that the electromagnetic wave is cut off inside the plasma [30]. The decay length δ (skin depth) basically depends on the coil frequency ω_{coil}, the electron-neutral collision frequency ν_{eff}, and the electron density n_e, and defines the power absorption region of the plasma. A detailed discussion can be found in the article of Vahedi *et al.* [13]. For the collisionless case ($\nu_{\mathrm{eff}} \ll \omega_{\mathrm{coil}}$) the skin depth is given by

$$\delta = \frac{c}{\omega_{\mathrm{pe}}} = \left(\frac{c^2 \epsilon_0 m_e}{e^2 n_e} \right)^{1/2}. \tag{2}$$

By using typical electron densities measured by LP (1×10^{11} to 3×10^{11} cm^{-3}) one gets decay lengths (power absorption regions) between 17 and 12 mm below the quartz vacuum interface. This corresponds to a distance of 23 to 32 mm above the lower electrode and agrees quite well with the region where the radial OES distribution shows a dependence on the coil geometry. Closer to the lower electrode, however, no dependence of the coil geometry is observed [see also Figs. 3(a) and 3(b)]. We attribute this to the rapid diffusion of the heated electrons, which are no longer influenced by induced rf electric fields but rather by dc electric fields created by diffusion.

B. Effect of an electrostatic shield and the electrical circuit on the radial plasma density distribution using the spiral coil

An electrostatic (Faraday) shield is known to reduce the capacitive coupling between the inductive coil and the plasma [8,22,31]. This shielding is important because the capacitive coupling component affects the ion energy so that adsorbed oxygen and other impurities can be released from the surface of the quartz interface window by ion bombardment. If there is already a thin film deposited on the inner

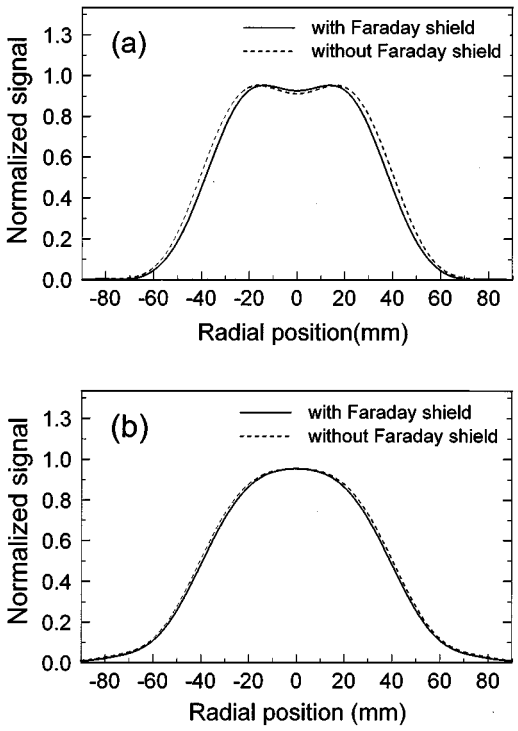

FIG. 8. Normalized Abel inverted OES signals with and without Faraday shield between (spiral) coil and plasma at a distance of (a) 33 mm and (b) 12 mm above the lower electrode ($P_{\mathrm{dis}}=50$ W, $p=1.33$ Pa).

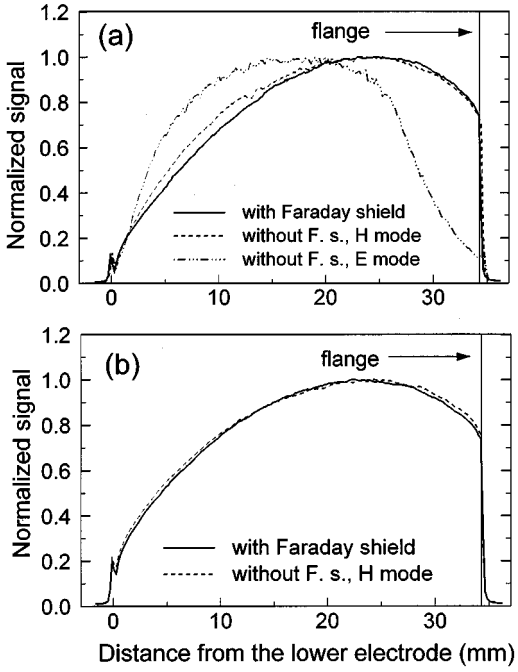

FIG. 9. Normalized line-of-sight-integrated OES signals with and without Faraday shield between coil and plasma vs distance from the lower electrode at (a) $P_{\mathrm{dis}}=24$ W and (b) $P_{\mathrm{dis}}=230$ W ($p=1.33$ Pa).

surface of the interface window this material can also be sputtered by ion bombardment and redeposited on the wafer. These sputtered impurities can also significantly change the plasma and etching chemistry [18].

The radial distribution of the OES signal is shown in Fig. 8 for the spiral coil at two different axial positions within the plasma. There is a slight difference between the shielded and nonshielded case at $z=33$ mm. For LP scans at $z=12$ mm the profiles with and without shielding practically overlap. Langmuir probe measurements have also been performed for the nonshielded case. A comparison of the LP data with the OES data at $z=12$ mm showed no difference within the uncertainty of the LP measurements. This implies that the electrostatic shield has little effect on the radial electron distribution. However, it does have an influence on the vertical OES distribution. At low plasma power, when the capacitive component of the power deposition is relatively strong, the relative OES signal in the discharge region close to the lower electrode is higher for the nonshielded case [see Fig. 9(a), which also contains the OES distribution of a dominantly capacitive or **E** mode discharge]. At higher plasma power, however, there is little difference in the vertical OES data distribution between the shielded and nonshielded case [Fig. 9(b)]. The rapid cutoff at the OES signal at ~ 34 mm is due to the obstruction from the stainless steel flange, which holds the quartz vacuum interface in place.

Model calculations for planar ICPs have shown that the azimuthal symmetry of the plasma can be strongly influenced by the circuit parameters of the coil [20,32]. Besides the amount of capacitive coupling from the coil to the plasma, the termination capacitance of the coil is of importance. Since the system behavior is analogous in some respects to that of a transmission line, the termination capacitance determines the location of the current maxima in the standing wave along the transmission line [32]. A change in the induced electric field and also in the power deposition should be observed when the termination reactance is of the order of the reactance Z of the coil ($Z=|i\omega L|\approx 94\ \Omega$). In order to investigate these effects, the outer lead of an electrostatically shielded, five-turn spiral coil was terminated with capacitances of 150 and 500 pF, corresponding to termination reactances ($Z_t=|i\omega C|^{-1}$) of ≈ 78 and $\approx 24\ \Omega$, respectively.

Since our Abel inversion technique assumes a symmetric plasma, any azimuthal asymmetries hidden in the line-of-sight-integrated OES data would be obscured by the Abel inversion process. Therefore, the line-of-sight-integrated OES data are presented in Fig. 10 for a coil with outer lead grounded and a coil with termination impedance of 500 pF. While the lateral scans are symmetric for all vertical positions in the case of a grounded coil, asymmetric lateral distributions are observed in the upper discharge region, close to the coil [see Fig. 10(b)], when the coil is terminated with an impedance of 150 or 500 pF. This asymmetry is more pronounced at higher plasma power. The corresponding azimuthal asymmetry, which causes the observed lateral asymmetries, cannot be calculated from our data. Full two-dimensional optical tomography is needed for this purpose and will be published separately. In the discharge region of the LP measurements and close to lower electrode symmetric lateral OES profiles were obtained (see Fig. 11). By compar-

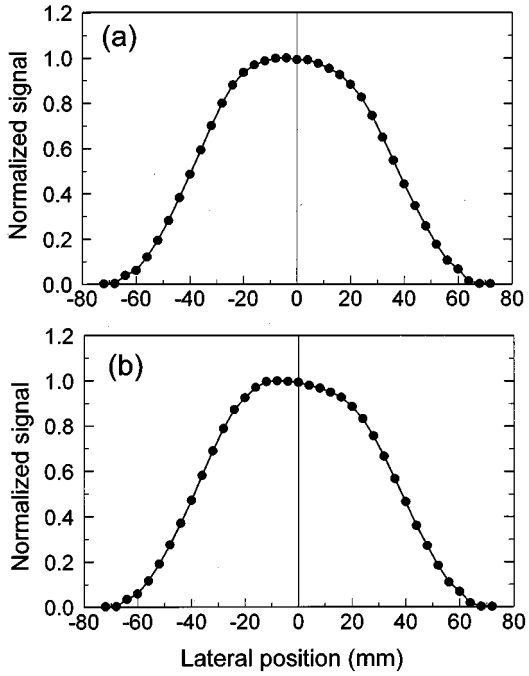

FIG. 10. Normalized line-of-sight-integrated OES signal at a distance of 33 mm above the lower electrode with (a) grounded outer lead of the spiral coil and (b) termination capacitance of 150 pF (P_{dis}=230 W, P=2.66 Pa).

ing the Abel inverted data only a minor influence of the termination on the radial plasma profile compared to a coil configuration with grounded outer lead was found.

Powering the outer lead of the spiral coil instead of the central lead has an observable effect on the radial OES distribution close to the coil [see Fig. 12(a)], while the distribution close to the lower electrode essentially remains unchanged [see Fig. 12(b)].

C. Effect of flow rate, plasma power, and gas pressure on the radial plasma density distribution

Another set of parameters was varied for the spiral coil with the electrostatic shield installed. Using different argon gas flow rates between 0.75 and 37.5 μmol/s (1–50 SCCM) we observed no flow rate dependence of the radial distribution for gas flow rates below 7.5 μmol/s (10 SCCM). However, at lower gas pressure [below about 1.33 Pa (10 mTorr)] and flow rates of 22.5 μmol/s (30 SCCM) and higher, the line-of-sight-integrated data become asymmetric, the maximum signal shifting towards the gas input side [see Fig. 13(a)]. In contrast to the capacitively coupled GEC RF Reference Cell, gas is fed into the discharge chamber not via holes in one electrode but via one of the 70 mm side flanges. The asymmetry observed at higher flow rates disappears at higher gas pressure [see Fig. 13(b)].

A plasma power variation between 62 and 209 W (corresponding to 100–300 W coil input power) at a fixed gas pressure resulted in an increase of the FWHM of the OES radial distribution at z=12 mm from 80 to 100 mm (see Fig. 14). A significant effect on the radial profile is also observed when running the discharge at different pressures. For pressures between 0.5 and 4 Pa the FWHM at z=12 mm decreases from 90 to 60 mm (see Fig. 15).

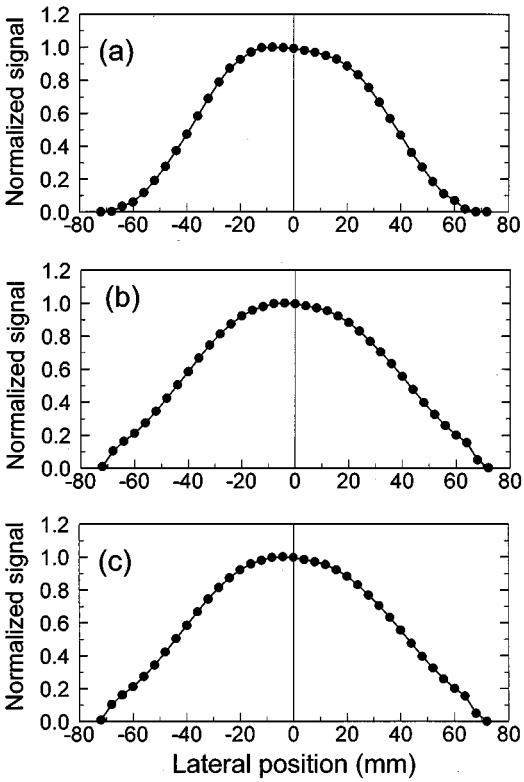

FIG. 11. Normalized line-of-sight-integrated OES signal at different distances from the lower electrode with a termination capacitance of 150 pF: (a) 33 mm, (b) 27 mm, and (c) 12 mm (P_{dis}=230 W, p=2.66 Pa).

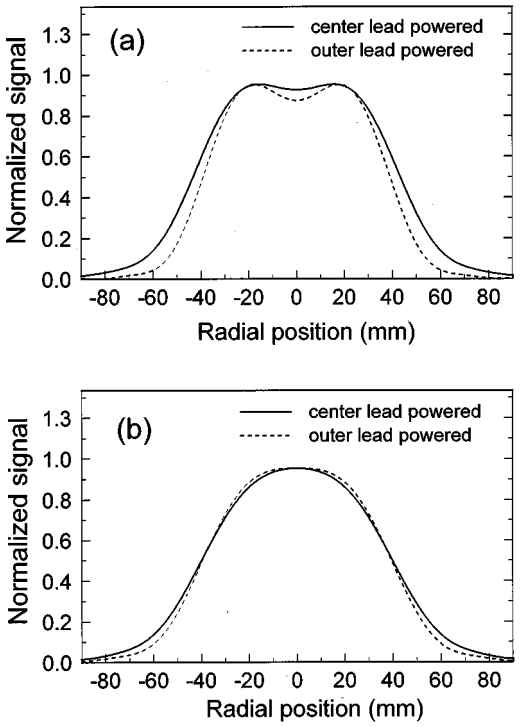

FIG. 12. Normalized Abel inverted OES signal at a distance of (a) 33 mm and (b) 12 mm above the lower electrode with either the center or outer lead of the spiral coil powered [p=1.33 Pa, P_{dis}=50 W (center) or 36 W (outer), respectively].

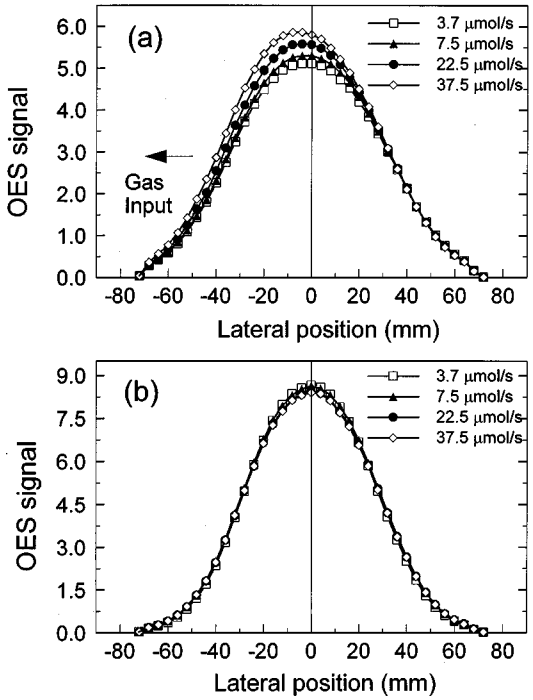

FIG. 13. Line-of-sight-integrated OES signal for different flow rates at a distance of 12 mm above the lower electrode at (a) $p = 1$ Pa and (b) $p = 2.66$ Pa ($P_{dis} = 50$ W).

IV. CONCLUSION

In this paper the radial distribution of the plasma density of a planar ICP using a modified GEC RF Reference Cell has been investigated by means of Langmuir probes and optical emission spectroscopy for different coil geometries, electrical circuit configurations and plasma parameters, e.g., total gas pressure and power dissipated into the plasma. We found that the coil geometry and electrical circuit configuration influences the radial plasma density distribution in the upper discharge region only, while in the region close to the lower electrode the radial profile is determined by diffusion. The measured bell-shaped radial OES distributions resemble distributions calculated by Allis and Rose [33,34] for plasmas where the radial distribution of charged particles is determined by the transition from ambipolar to free diffusion. Pure ambipolar diffusion would result in a Bessel-shaped profile [13,35], which is not observed in our setup.

A unique feature of the GEC-ICP cell is the relatively small ratio of the induction coil diameter compared to the chamber diameter (0.40). Taking into account the two large observation window flanges (diameter 203 mm, length 70 mm) and the other six diagnostic flanges, the effective ratio is estimated to be of the order of 0.30. Table I gives a dimensional overview of different planar ICP reactor types. We infer that this ratio and also the distance between quartz vacuum interface and lower electrode play a key role for the radial plasma distribution for this type of reactor without

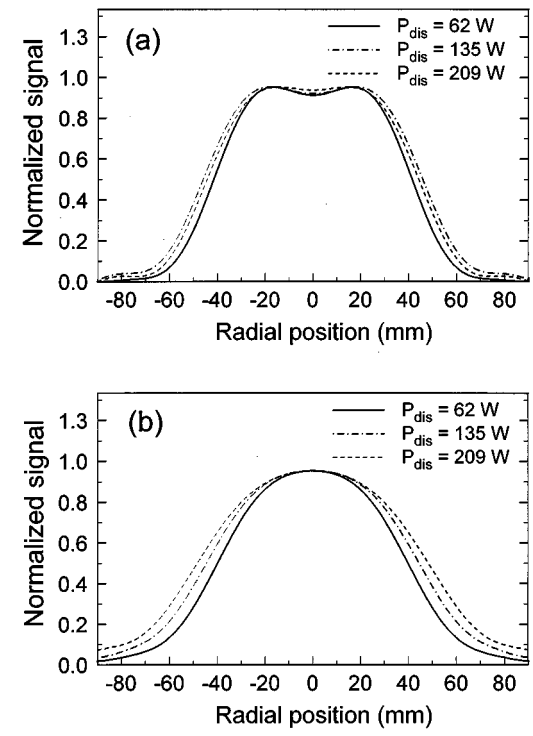

FIG. 14. Normalized Abel inverted OES signal at a distance of (a) 33 mm and (b) 12 mm above the lower electrode at different plasma powers ($p = 1.33$ Pa).

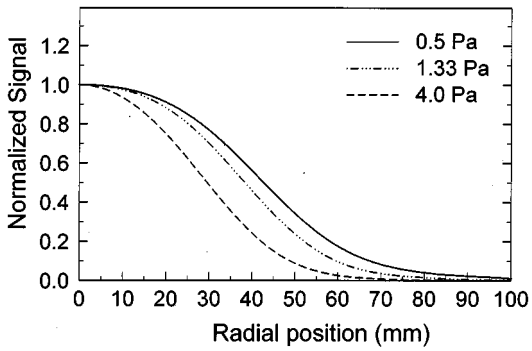

FIG. 15. Normalized Abel inverted OES signal at a distance of 12 mm above the lower electrode at different pressures.

TABLE I. Comparison of cell and coil geometries of different planar ICPs.

Reference	Cell diameter d_{cell} (mm)	Coil diameter d_{coil} (mm)	Ratio d_{coil}/d_{cell}	Coil to lower electrode distance (mm)
[4,36]	250	225	0.90	34
[15]	270[a]	240	0.89	25–130[c]
[41]	340	280[b]	0.82	25–120[c]
[22]	228	165	0.72	169
[42]	300	200	0.67	100
[43]	300	184	0.61	65–180[c]
[19]	310	160[b]	0.52	50
This work, [6]	251	100	0.40	53 (50)

[a]Square chamber and square coil geometry.
[b]One-turn coil.
[c]Mobile lower electrode.

permanent magnets. The ratio of coil diameter to the cell diameter should be close to one, similar to the commercial etching system used by Carter *et al.* [4] and later modeled by Hoekstra and Kushner [36]. The induction coil diameter should probably be larger than the wafer diameter. Another unique feature of the GEC-ICP cell is that the induction coil is surrounded by a stainless steel tube whose inner diameter is just several mm larger than the coil diameter, thus inducing considerable image currents in the cylinder walls. These image currents are likely to have an effect on the plasma.

Our results may indicate that it could be advantageous to reduce the distance between the quartz vacuum interface and lower electrode or substrate. However, in commercial etching devices this distance has to be of the order of several skin depths, otherwise the induced electric and magnetic fields in the plasma region close to the quartz vacuum interface may cause damage to the substrate [37].

In summary, we conclude that for the discharge cell investigated in this work, i.e., a modified GEC RF Reference Cell (GEC-ICP cell), it is not possible to achieve a better radial uniformity by changing the coil configuration or power configuration of the coil. The existing published 2D simulations for the GEC-ICP cell (see, for example, Refs. [38–40]) reproduce the observed radial profiles quite well for a nonshielded, five-turn spiral coil with grounded outer lead. To our knowledge no calculations have been made for a one-turn coil and the different electrical circuit configurations investigated in this work. Such calculations would give further insight into the discharge physics of the GEC-ICP cell.

ACKNOWLEDGMENT

One of the authors (A.S.) was sponsored by the Alexander von Humboldt Foundation.

[1] D. K. Coultas and J. H. Keller, European Patent Application No. 0379828A2 (1990).
[2] J. S. Ogle, U.S. Patent No. 4.948.458 (1990).
[3] J. Hopwood, Plasma Sources Sci. Technol. **1**, 109 (1992).
[4] J. B. Carter, J. P. Holland, E. Peltzer, B. Richardson, E. Boyle, H. T. Nguyen, Y. Melaku, D. Gates, and M. Ben-Dor, J. Vac. Sci. Technol. A **11**, 1301 (1993).
[5] P. J. Hargis, Jr., K. E. Greenberg, P. A. Miller, J. B. Gerado, J. R. Torczyinski, M. E. Riley, G. A. Hebner, J. R. Roberts, J. K. Olthoff, J. R. Whetstone, R. H. Van Brunt, M. A. Sobolewski, H. M. Anderson, M. P. Splichal, J. L. Mock, P. Bletzinger, A. Garscadden, R. A. Gottscho, G. Selwyn, M. Dalvie, J. E. Heidenreich, J. W. Butterbaugh, M. L. Brake, M. L. Passow, J. Pender, A. Lujan, M. E. Elta, D. B. Graves, H. H. Sawin, M. J. Kushner, J. T. Verdeyen, R. Horwath, and T. R. Turner, Rev. Sci. Instrum. **65**, 140 (1994).
[6] P. A. Miller, G. A. Hebner, K. E. Greenberg, P. D. Pochan, and B. P. Aragon, J. Res. Natl. Inst. Stand. Technol. **100**, 427 (1995).
[7] G. A. Hebner, J. Vac. Sci. Technol. A **14**, 2158 (1996).
[8] A. Schwabedissen, E. C. Benck, and J. R. Roberts, Phys. Rev. E **55**, 3450 (1997).
[9] E. C. Benck, A. Schwabedissen, A. Gates, and J. R. Roberts, J. Vac. Sci. Technol. A (to be published).
[10] J. H. Keller (unpublished); Abstracts of the 42nd Gaseous Electronics Conference, Berkeley, CA, 1989, Paper QA 5 (unpublished).
[11] P. L. G. Ventzek, R. J. Hoekstra, T. J. Sommers, and M. J. Kushner, Appl. Phys. Lett. **63**, 605 (1993).
[12] M. M. Turner, Phys. Rev. Lett. **71**, 1844 (1993).
[13] V. Vahedi, M. A. Lieberman, G. DiPeso, T. D. Rognlien, and D. Hewett, J. Appl. Phys. **78**, 1446 (1995).
[14] J. H. Keller, J. C. Forster, and Michael S. Barnes, J. Vac. Sci. Technol. A **11**, 2487 (1993).
[15] J. Hopwood, C. R. Guarnieri, S. J. Whitehair, and J. J. Cuomo, J. Vac. Sci. Technol. A **11**, 152 (1993).
[16] C. Lai, B. Brunmeier, and R. Claude Woods, J. Vac. Sci. Technol. A **13**, 2086 (1995).
[17] C.-H. Chen, D. Liu, and D. Tran, U.S. Patent No. 5.226.967 (1993).
[18] K. Yoshida, H. Miyamoto, E. Ikawa, and Y. Murao, Jpn. J. Appl. Phys., Part 1 **34**, 2089 (1995).
[19] T. Fukasawa, T. Nouda, A. Nakamura, H. Shindo, and Y. Horiike, Jpn. J. Appl. Phys., Part 1 **32**, 6076 (1993).
[20] M. J. Kushner, W. Z. Collision, M. J. Grapperhaus, J. P. Holland, and M. S. Barnes, J. Appl. Phys. **80**, 1337 (1996).
[21] G. Mümken and U. Kortshagen, J. Appl. Phys. **80**, 6639 (1996).
[22] L. J. Mahoney, A. E. Wendt, E. Barrios, C. J. Richards, and J. L. Shohet, J. Appl. Phys. **76**, 2041 (1994).
[23] H. J. Druyvesteyn, Z. Phys. **64**, 781 (1930).
[24] V. A. Godyak, R. B. Piejak, and B. M. Alexandrovich, J. Appl. Phys. **73**, 3657 (1993).
[25] G. Pretzler, H. Jäger, T. Neger, H. Philipp, and H. Woisetschläger, Z. Naturforsch. Teil A **47**, 955 (1992).
[26] G. A. Hebner, J. Appl. Phys. **80**, 2624 (1996).
[27] W. L. Wiese, M. W. Smith, and B. M. Miles, *Atomic Transition Probabilities, Vol. II*, NSRDS-NBS No. 22 (U.S. GPO, Washington, DC, 1969).
[28] R. E. H. Clark, J. B. Mann, G. Csanak, and A. L. Merls (unpublished).
[29] J. Hopwood, C. R. Guarnieri, S. J. Whitehair, and J. J. Cuomo, J. Vac. Sci. Technol. A **11**, 147 (1993).
[30] J. D. Jackson, *Classical Electrodynamics*, 1st ed. (Wiley, New York, 1965).
[31] H. Sugai, K. Nakamura, and K. Suzuki, Jpn. J. Appl. Phys., Part 1 **33**, 2189 (1994).
[32] E. F. Jaeger, L. A. Berry, J. S. Tolliver, and D. B. Batchelor, Phys. Plasmas **2**, 2597 (1995).
[33] W. P. Allis and D. J. Rose, Phys. Rev. **93**, 84 (1954).
[34] S. C. Brown, *Basic Data of Plasma Physics* (Wiley, New York, 1959), pp. 91–95.
[35] W. Schottky, Phys. Z. **25**, 635 (1924).
[36] R. J. Hoekstra and M. J. Kushner, J. Appl. Phys. **79**, 2275 (1996).
[37] J. H. Keller, Plasma Sources Sci. Technol. **5**, 166 (1996).
[38] R. S. Wise, D. P. Lymberopoulos, and D. J. Economou, Appl. Phys. Lett. **68**, 2499 (1996).

[39] J. D. Bukowski, B. D. Graves, and P. Vitello, J. Appl. Phys. **80**, 2614 (1996).

[40] M. J. Grapperhaus and M. J. Kushner, J. Appl. Phys. **81**, 569 (1997).

[41] D. F. Beale, V. I. Kolobov, J. A. Stittsworth, W. N. G. Hitchon, and A. E. Wendt, Proceedings of the IEEE Conference on Plasma Science, Madison, WI, 1995 (IEEE, New York, 1996).

[42] T. Hori, M. D. Bowden, K. Uchino, and K. Muraoka, Appl. Phys. Lett. **69**, 3683 (1996).

[43] P. N. Wainman, M. A. Lieberman, A. J. Lichtenberg, R. A. Stewart, and C. Lee, J. Vac. Sci. Technol. A **13**, 2464 (1995).